Ritter Island Volcano—lateral collapse and the tsunami of 1888

Steven N. Ward[1] and Simon Day[2]

[1]*Institute of Geophysics and Planetary Physics, University of California, Santa Cruz,* CA 95064, *USA. E-mail: ward@es.ucsc.edu*
[2]*Benfield Hazard Research Centre, Department of Earth Sciences, University College, London, Gower Street, London* WC1E 6BT.
E-mail: s.day@ucl.ac.uk

SUMMARY

In the early morning of 1888 March 13, roughly 5 km^3 of Ritter Island Volcano fell violently into the sea northeast of New Guinea. This event, the largest lateral collapse of an island volcano to be recorded in historical time, flung devastating tsunami tens of metres high on to adjacent shores. Several hundred kilometres away, observers on New Guinea chronicled 3 min period waves up to 8 m high, that lasted for as long as 3 h. These accounts represent the best available first-hand information on tsunami generated by a major volcano lateral collapse. In this article, we simulate the Ritter Island landslide as constrained by a 1985 sonar survey of its debris field and compare predicted tsunami with historical observations. The best agreement occurs for landslides travelling at 40 m s^{-1}, but velocities up to 80 m s^{-1} cannot be excluded. The Ritter Island debris dropped little more than 800 m vertically and moved slowly compared with landslides that descend into deeper water. Basal friction block models predict that slides with shorter falls should attain lower peak velocities and that 40+ m s^{-1} is perfectly compatible with the geometry and runout extent of the Ritter Island landslide. The consensus between theory and observation for the Ritter Island waves increases our confidence in the existence of mega-tsunami produced by oceanic volcano collapses two to three orders of magnitude larger in scale.

Key words: landslides, tsunami, volcano collapse.

1 THE LARGEST ISLAND VOLCANO COLLAPSE IN HISTORICAL RECORDS: A TEMPLATE FOR MEGA-SLIDES?

Ritter Island, one of a group of volcanic islands between New Britain and New Guinea (Fig. 1), collapsed on 1888 March 13, around 5:30 am local time (Cooke 1981). The collapse reduced the 780 m high, 1.5 km wide island to a thin crescent-shaped remnant and excavated much of the western submarine flank of the volcano (Johnson 1987). As much as 5 km^3 of material mobilized (twice the volume of the 1980 collapse of Mount St Helens). The westward-directed landslide launched a catastrophic tsunami that first struck adjacent coasts where several hundred people may have perished, then spread further, inflicting significant damage on islands out to several hundred kilometres (Cooke 1981).

The year 1888 fell in the first decade of colonization of the New Guinea archipelago by Germany. For this reason, accounts of this remote volcano collapse and tsunami exist from a handful of western settlements. Critically, the tsunami was observed at these settlements by individuals with pocket watches. Watches enable and habituate people to mark time intervals as short as minutes, so eyewitness accounts of the Ritter Island tsunami include estimates of the wave period and wave arrival time, as well as wave amplitude. This circumstance contrasts earlier historical stratovolcano collapses where only wave runup observations were recorded (notably Oshima Oshima volcano in the Sea of Japan in 1741; Satake & Kato 2001).

In this article, we develop landslide simulations scaled to the parameters of the Ritter Island collapse and compare the predicted tsunami with historical observations. In previous works (Ward 2001; Ward & Day 2001; Ward 2002a) we modelled tsunami from the 1.8 Myr old (Kanamatsu *et al.* 2002) Nuaanu collapse on Oahu, and from hypothetical volcano collapses at La Palma and Kilauea. The volumes of these collapses exceed the Ritter Island event by two or three orders of magnitude. Here, we test our theory by seeing if it scales successfully to a much smaller collapse; in particular, to the prediction of the tsunami waves that impacted the coasts around Ritter Island on 1888 March 13.

2 OBSERVATIONS AND INFERENCES CONCERNING THE TSUNAMI, THE COLLAPSE AND THE LANDSLIDE DEPOSITS

Contemporary observations

Table 1 summarizes the tsunami accounts of which there are two types: (1) direct eyewitness reports of the waves and (2) subsequent damage observations on nearby coasts. The former come from

Table 1. Summary of direct eyewitness reports and subsequent observations of damage (see Cooke 1981, for a more complete version). Locations are indicated in Fig. 1.

Location and type of observations	Time of first wave arrival; duration of wave arrivals	Observed wave periods	Wave amplitudes or runups/inundations
Finschafen (E)	Soon after 6.30 am; 30 min of strong irregular waves	3–4 min	Initial drawdown 1.5–2 m in 2 min
Kelana (E)	6.30 am; 1 h of observed strong waves	3 min (20 waves in total)	Runup of first wave 8 m; runup of fourth wave 10 m
Hatzfeldhafen (E)	6.40 am; 2.5 h of strong wave motions.	3–4 min	Initial rise >2 m above high tide; peak wave height (8 am) 7–8 m
Umboi I., N & E coasts (D)	—	—	Coastal zone stripped to *ca.* 15 m a.s.l.
Sakar I. (D)	—	—	Coastal zone stripped to *ca.* 15 m a.s.l.
New Britain (east coast of Dampier Strait) (D)*	Before 6 am	—	Destruction and tsunami deposits extending c. 1 km inland and flood-marks on trees to 12–15 m a.s.l. 4.5 m maximum runup
Matupi, Rabaul (E)	8.15 am; 3 h of observed waves		

(E = eyewitness; D = subsequent damage report; a.s.l = above sea level).
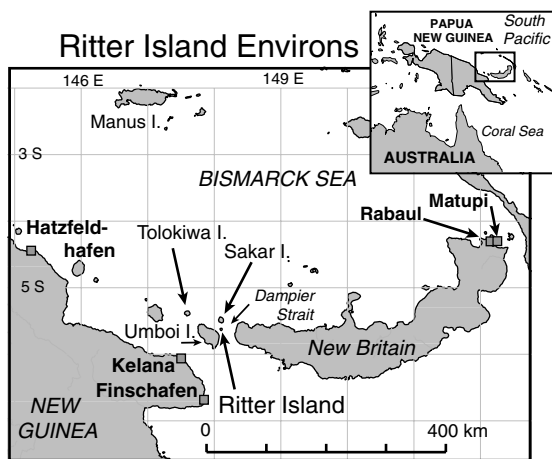*Survivors of an expedition caught by the tsunami on this coast reported the arrival of the tsunami before daybreak.

Figure 1. Location of New Britain/New Guinea area (inset). Principal islands and tsunami observation points (squares) are marked.

mission sites of Hatzfeldhafen, Kelana and Finschafen on New Guinea (Fig. 1) while the latter come from the islands of Umboi and Sakar and the western end of New Britain. By and large, the observed waves at the mission sites reached 8 m height. None of these locations, however, had a direct 'line of sight' to Ritter Island so the observed waves must have reflected or diffracted around intervening islands. These are not efficient processes, so unobstructed sites at the same distance should have seen larger waves.

The subsequent damage observations include those made immediately after the collapse during the search for a German expedition caught by the tsunami on New Britain, and observations made 1 or 2 years later of the coasts of Sakar and Umboi from the decks of ships at sea. The direct onshore observations in New Britain accurately fix both inundation height (∼15 m) and inundation distance (∼1 km) there. However, the heights (∼15 m) of the zones of complete vegetation stripping on Sakar and Umboi as seen from offshore probably understate the true limits because palms and other trees along tropical coasts can withstand several metres of inundation by turbulent bores (e.g. the 1998 Sissano tsunami, Kawata

et al. 1999; McSaveney *et al.* 2000; Davies *et al.* 2003). The true inundation heights on Sakar and Umboi Islands may have exceeded 20 m.

Other aspects apparent from the eyewitness accounts are the short period of tsunami waves and the long duration of the tsunami as a whole. Observers at Hatzfeldhafen and Kelana emphasized a 3–4 min period, whereas typical earthquake-generated tsunami have 10–15 min wave periods. At Finschafen too, the initial wave cycle took about 4 min, although later motion was described as 'irregular'. All eyewitnesses reported a large number of waves with rapid sea surface movements lasting longer at more distant sites (30 min at Finschafen, 1 h at Kelana, 2.5 h at Hatzfeldhafen and nearly 3 h at Matupi). We believe that the collapse itself produced the short-period waves. If they were artefacts of local harbour resonance for instance, the frequencies would differ between sites. The short wave period means that wave dispersion effects will be crucial in modelling tsunami of the event. A characteristic feature of dispersion, the stretching out of the tsunami with time as different frequency components travel at different speeds, seems manifest in the observation that tsunami duration increased with distance. Recognizing the Ritter Island tsunami waves to be short period also bears on the interpretation of the subsequent damage. Many of the coasts that suffered runup damage lie flat with fringing reefs. Penetration inland and up slope for 3–4 min waves may be limited more by the rapid onset of backwash as the next wave trough arrives than by the actual height of the wave crests.

The eyewitness accounts also underscore the lack of explosive activity accompanying the collapse of the volcano. Although residents noted sounds of explosions and saw an 'almost imperceptible' ash fall at Finschafen (Cooke 1981), explosive activity was very minor compared with the eruption at Krakatoa in 1883. Johnson (1987) associated the accounts of explosions at Ritter Island with phreatic activity caused by explosive decompression of a hydrothermal system or a small magma body as the summit of the volcano slid away. Such explosions could not have contributed much to the tsunami, so sea wave generation models for the Ritter Island collapse can be simpler than for the Krakatoa eruption (Simkin & Fiske 1983). Tsunami there may have been produced by complex episodes of caldera collapse, lateral collapses of the caldera walls and massive pyroclastic flows entering the sea (Latter 1981; Self & Rampino 1981).
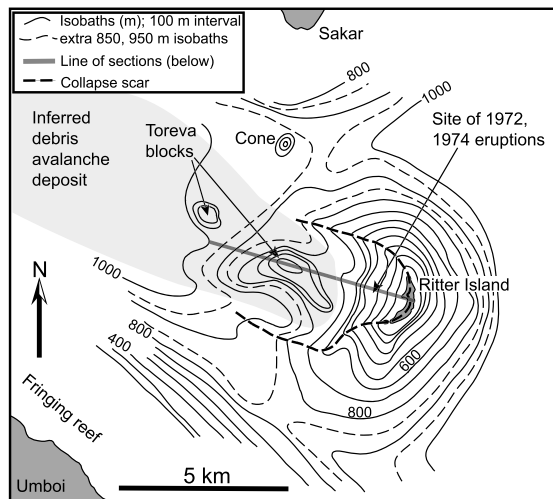
Figure 2. Geometry of the present-day collapse scar at Ritter Island (after Johnson 1987) showing the toreva blocks in the mouth of the horseshoe-shaped collapse scar and the elongated conical shape of the remaining flanks of the Ritter Island volcano.

Subsequent observations

Nearly a century after the Ritter Island collapse, R.W. Johnson surveyed the scar and the proximal part of the landslide using a commercial single-beam echo sounder mounted on a schooner borrowed from an archaeological research project (Johnson 1987). His survey (Fig. 2) identified a submerged WNW-facing amphitheatre 3.5 km wide and more than 4 km from mouth to headwall, the arcuate crest of which forms the western side of Ritter Island itself. At the mouth of the collapse scar, the survey located flat-topped mounds up to 2 km long, rising hundreds of metres above the surrounding sea floor. Johnson interpreted these as slide blocks or torevas. The depth limitations of the echo sounder prevented mapping of the distal part of the collapse, but deposits there must be extensive because little of the 4–5 km³ of slide material estimated by Johnson remains within the area surveyed.

The collapse scar and collapse deposit geometries: observations and inferences

Early visitors to the region described pre-collapse Ritter Island as notably steep, rising as much as 780 m above sea level while being less than 1.5 km wide (Cooke 1981). Its topography was not recorded in detail, however, and nothing is known concerning pre-collapse submarine topography anywhere around the Island. Extrapolation of pre-collapse profiles from the broadly conical slopes that remain to the north and south reveals a 500–600 m depth difference between the pre-collapse surface and the present-day floor of the amphitheatre along its axis. This height difference probably corresponds to the maximum thickness of the slide at its centre. The collapse scar has been partly filled with the products of later eruptions (notably in 1972 and 1974, Cooke 1981), so the initial depth of the scar floor and the actual thickness of the landslide may have been greater. A ~500 m slide thickness is also indicated by the height of the largest toreva in the mouth of the collapse scar above its surrounding. Even allowing for the thinning of the slide mass toward the sides of the scar, we find it difficult to reduce the volume of the landslide below Johnson's 4–5 km³ maximum. Although the distal part of the

debris deposit was not mapped by Johnson, analogies can be drawn with the completely mapped avalanches at Oshima Oshima (Satake & Kato 2001) and other subaerial stratovolcanoes (Ui *et al.* 1986; Siebert *et al.* 1987). We suggest that 4–5 km³ of the Island's debris forms a deposit that extends down the axis of the channel between Umboi and Sakar Islands as far as 20 km from Ritter, and has a width of about 5 km (shaded area, Fig. 2).

Inferred kinematic history of the collapse

No eyewitness observations of the collapse exist, so like landslide volume and extent, a kinematic history must be inferred. A good analogue might be the first stages of the similarly sized Mount St Helens collapse (Voight 1981; Voight *et al.* 1983). If so, the failing flank of Ritter volcano initially slid for a kilometre or two in one or a few large blocks that experienced limited internal strain (otherwise the toreva would not have survived intact). We propose that, upon arriving at the site of the toreva field, the slide block disintegrated into a debris avalanche composed of smaller blocks of a variety of sizes. While the larger pieces grounded and stopped, the remainder of the mass disintegrated into a thinner sheet that ran between Sakar and Umboi Islands towards the deep water of the Bismarck Sea. Fig. 3 depicts this concept of the kinematic history of the Ritter Island landslide as deduced from both measured and inferred information.

3 THE LANDSLIDE MODEL

To compute the sea waves from the Ritter Island collapse, the concept in Fig. 3 must be adapted to the framework of our landslide tsunami model (Ward 2001). For this, we divide the landslide area into cells that excavate or fill to specified depths in a predetermined sequence. Typically, cells in the collapse scar excavate, cells in the middle of the landslide may fill and then excavate, and cells in the distal areas only fill. The sequence is defined by sets of cells that start to excavate or fill to a given depth at a given time step (Fig. 4). Spanning one or more time steps from that start, the cells then excavate or fill progressively from their upslope or downslope edge, respectively. The cell fill and excavation thicknesses, start times and fill spans, together with the actual duration of the time step fix the kinematics of the landslide model.

We constrain the sequence of cell filling and emptying as follows. First, because the existence of large toreva near the mouth of the 1888 scar indicates initial block-like sliding, the cells in the first few steps in the sequence excavate and fill in block-like fashion. Secondly, because the toreva did become stranded, transport of material beyond there must have been heterogeneous. Thus, the sliding phase was followed by progressive disintegration in the vicinity of the toreva field from where the debris spread downslope as a thin sheet. These latter stages are modelled by progressive excavation of the cells that were filled during the sliding phase and volume-balancing the successive filling of cells further downslope. We excavate the cells near the toreva blocks so that they retain their maximum thickness until close to the end of the landslide history. The cross-section and plan view in Fig. 4 portray the Ritter landslide as seen through the lens of the model. The bottom panel lists the net excavation or fill thickness of each cell. In the absence of detailed information on lateral thickness variations in the deposit, we took a uniform thickness of excavation and deposition across the slide. Note that for all but the uppermost two rows of cells, excavation and fill thicknesses are small fractions of the local water depth, so non-linear wave effects
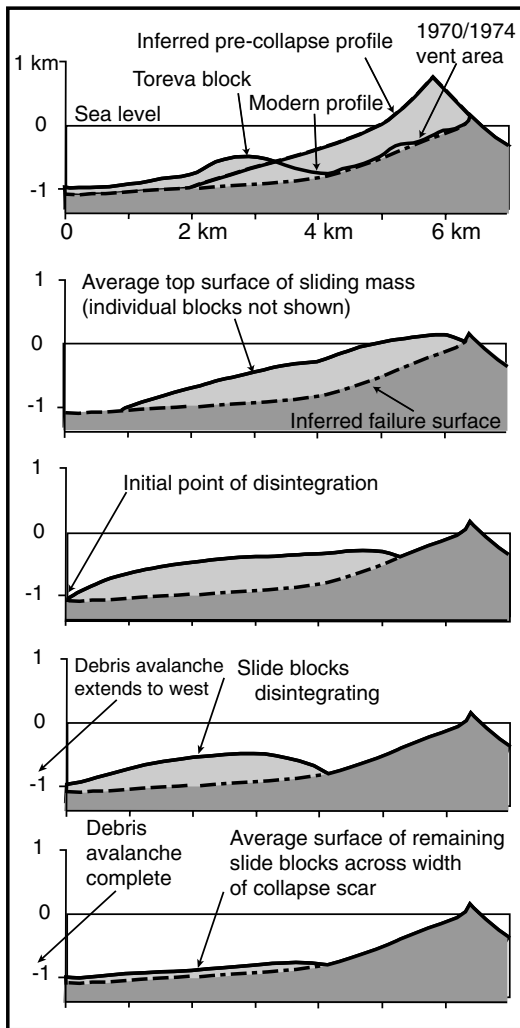
Figure 3. Inferred history of the Ritter Island landslide during the first stages of the collapse, showing the evolution of the landslide from sliding blocks to a debris avalanche that leaves behind stranded toreva blocks. The 'modern profile' in the top panel is drawn over one of the stranded blocks. The bottom four panels sketch the average slide thickness, so the blocks do not appear in these.

should not be strong. The total landslide volume in the model is 4.6 km³.

The last element of the landslide model assigns real time units to the cell starts and step duration. Rather than attempting to define complex kinematic histories for which no direct constraints exist, we run a series of constant-velocity runout models that bracket a range of likely speeds. (Actually, these models involve several different speeds, all less than the runout speed referred to here.) Constant-speed runouts may not be an unrealistic approximation. The steep initial basal slope (10°–15° average, 25° peak) should make for a short-lived acceleration phase. Then, facing a decreasing basal slope, the slide might spend much of the reminder of its movement history travelling at a limiting speed. (Frictional landslide models in Section 7 quantify this thinking.) The time and velocity numbers in Fig. 4 show a 40 m s⁻¹ landslide that takes about 5 min to run its course.
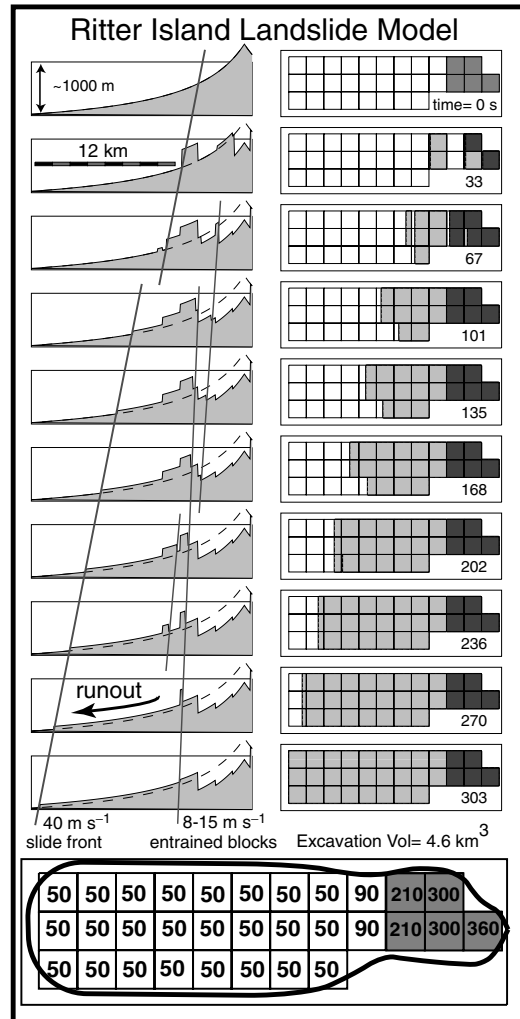

Figure 4. The Ritter Island landslide model in plan (right) and section (left) view, orientated along bearing 290°. The section view has considerable vertical exaggeration. Dark cells (1.5 km on a side) in plan view indicate areas of net filling, grey cells indicate areas of net excavation. Depths of net filling or excavation in metres are listed in the bottom panel.

Landslide energy

Landslides release gravitational potential energy as they fall. For island collapses into the ocean, a fraction of the released energy goes to raise the displaced water. The total energy available for other purposes amounts to

$$E_{\rm L} = g \int_{\mathbf{r}} dA(\mathbf{r})\rho_{\rm eff}(\mathbf{r})\Delta u(\mathbf{r})h(\mathbf{r}). \qquad (1)$$

Here, $g = 9.8$ m s⁻², $h(\mathbf{r})$ is the depth below sea level (taken as positive downward) and $\Delta u(\mathbf{r})$ is the excavation or deposition thickness (excavation negative). The integral covers all of the area where $\Delta u(\mathbf{r}) \neq 0$. $\rho_{\rm eff}(\mathbf{r})$ is the effective density of the column of slide material at $\mathbf{r}$. $\rho_{\rm eff}(\mathbf{r})$ equals $\rho_{\rm s}$, the density of the slide material (2.5 gm cm⁻³), for subaerial columns ($h(\mathbf{r}) < 0$). $\rho_{\rm eff}(\mathbf{r})$ equals ($\rho_{\rm s} - \rho_{\rm w}$) for fully submerged columns ($h(\mathbf{r}) > |\Delta u(\mathbf{r})| > 0$). For partly submerged columns ($|\Delta u(\mathbf{r})| > h(\mathbf{r}) > 0$), $\rho_{\rm eff}(\mathbf{r})$ equals $\rho_{\rm s} - \rho_{\rm w}h(\mathbf{r})/|\Delta u(\mathbf{r})|$. $E_{\rm L}$ fixes the energy budget of all landslide processes. The energy of radiated tsunami and all manner of frictional losses draw from this pool (tsunami generated during landslides can be considered as

a frictional loss). Note that E_L depends only on the initial and final state of the slide, not its entire kinematic history. The Ritter Island collapse model released 2.0×10^{16} J of available energy.

4 THE TSUNAMI MODEL

Having specified the Ritter Island landslide model, we calculate the induced tsunami using the theory of Ward (2001) that views landslide sources as equivalent vertical displacements of the sea floor. Under this theory in a uniform ocean of depth h, a vertical bottom disturbance $u_z^{\text{bot}}(\mathbf{r}, t)$ starting at $t = 0$ stimulates surface tsunami waveforms (vertical component) at observation point $\mathbf{r}$ of

$$u_z^{\text{surf}}(\mathbf{r}, t) = \int_0^\infty \frac{d\omega k(\omega)}{2\pi u(\omega) \cosh(k(\omega)h)} \int_{A(t)} d\mathbf{r}_0 J_0(k(\omega)|\mathbf{r} - \mathbf{r}_0|)$$
$$\times \int_0^t dt_0 \dot{u}_z^{\text{bot}}(\mathbf{r}_0, t_0) \cos[\omega(t - t_0)]. \qquad (2)$$

In eq. (2), k is the wavenumber, ω is the frequency $\omega(k) = \sqrt{gk \tanh(kh)}$, $d\mathbf{r}_0 = dx_0 \, dy_0$, a dot represents $\partial/\partial t$ and $J_0(x)$ is the cylindrical Bessel function of order zero. The second integral covers the landslide area $A(t)$. Linear tsunami theory, eq. (2), is fully 3-D, and neither depth-averaged nor restricted to long or short waves. The seafloor displacement function $u_z^{\text{bot}}(\mathbf{r}_0, t)$ takes any shape, thickness, slide velocity, slide direction and time history needed to replicate landslide kinematics.

To help evaluate the last two integrals in eq. (2), we divide the landslide region into N square cells as described in the previous section and place in them, one or more simple slides. A simple slide has a constant excavation or fill thickness Δu, and a step function time dependence. At $t_0 = 0$, the simple slide starts along the upslope width of the cell centred at $\mathbf{r}_0$ and runs down at velocity v_r. If the observation point is not too close to the cell, and $t > L/v_r$, then eq. (2) becomes in a non-uniform depth ocean,

$$u_z^{\text{surf}}(\mathbf{r}, t) \approx \frac{\Delta u L^2}{2\pi}$$
$$\times \sum_{\text{all } N \text{ cells}} \int_0^\infty d\omega \frac{k_0(\omega) J_0(\omega T(\omega, \mathbf{r}, \mathbf{r}_0)) \cos[\omega t + X(\omega, \theta)]}{u_0(\omega) \cosh[(k_0(\omega)h(\mathbf{r}_0)]}$$
$$\times \frac{\sin X(\omega, \theta)}{X(\omega, \theta)} \frac{\sin Y(\omega, \theta)}{Y(\omega, \theta)} G(\mathbf{r}, \mathbf{r}_0) S_L(\omega, \mathbf{r}, \mathbf{r}_0), \qquad (3)$$

where $X(\omega, \theta) = L(k_0(\omega) \cos\theta - \omega/v_r)/2$; $Y(\omega, \theta) = W(k_0(\omega) \sin\theta)/2$, and θ is the angle between the slide direction and the observation point. $k_0(\omega)$ and $u_0(\omega)$ are the wavenumber and group velocity now specific to frequency ω in water of depth $h(\mathbf{r}_0)$. Eq. (3) supposes that within each cell $h(\mathbf{r}_0)$ is constant, but it does vary from cell to cell over the slide region. The new terms $T(\omega, \mathbf{r}, \mathbf{r}_0)$, $G(\mathbf{r}, \mathbf{r}_0)$ and $S_L(\omega, \mathbf{r}, \mathbf{r}_0)$ in eq. (3) account for changes in traveltime, and wave height due to geometrical spreading and shoaling in oceans of variable depth. These terms are ray-theory-based and their functional form can be found in Ward (2001). In overview, the process of generating landslide tsunami involves computing the integral (3), appropriately shifted in space and time to match each 'fill' or 'excavation', for all N cells in the model for every observation point of interest.

The principal advantages of this approach to landslide tsunami calculation are that: (1) detailed and time-evolving slide histories can be accommodated (not just initial sea surface 'lumps') and (2) full account of frequency dispersion is taken. Tsunami produced by kilometre-scale landslides, such as the Ritter Island event, have dominant wave periods (Ward 2002b) of 100–300 s. Dispersion

is strong at these periods, and by spreading out wave energy, it limits tsunami damage especially at larger distances. Long-wave or shallow-water techniques developed to model longer-period tsunami from earthquakes or mega-scale landslides (e.g. Aida 1978; Satake 1987; Johnson & Satake 1996; Satake *et al.* 2002) ignore dispersion. While frequency-dependent dispersion may be negligible at wave periods >1000 s, long-wave techniques are not credible for modelling shorter-period tsunami such as those produced by Ritter-sized volcano collapses.

The principal disadvantage of the present approach is that we calculate $T(\omega, \mathbf{r}, \mathbf{r}_0)$, $G(\mathbf{r}, \mathbf{r}_0)$ and $S_L(\omega, \mathbf{r}, \mathbf{r}_0)$ using single rays. In doing so, locations affected by tsunami must have a line of sight to some part of the landslide. Without wave diffraction and reflection, many places lie in artificial shadows. For landslides that locate near adjacent islands, this disadvantage is especially evident. In fact, all of the eyewitness reports of the Ritter Island tsunami come from sites on the coast of New Guinea that lie in ray shadows. To make comparisons in Section 6, we resort to 'proxy' locations near the observation sites that have some view of the slide.

Tsunami envelope

Contouring tsunami height can make for nearly unreadable regional maps due to the small distances that separate successive waves. Instead we plot $E_z^{\text{surf}}(\mathbf{r}, t)$, the tsunami envelope. The envelope acts like a sheet draped over the oscillating wave train. It tracks the evolving amplitude of the train without the distraction of many swings in sign. The envelope

$$E_z^{\text{surf}}(\mathbf{r}, t) = \left\{ \left[u_z^{\text{surf}}(\mathbf{r}, t) \right]^2 + \left[H_z^{\text{surf}}(\mathbf{r}, t) \right]^2 \right\}^{1/2} \qquad (4)$$

has units of metres. $H_z^{\text{surf}}(\mathbf{r}, t)$, the Hilbert transform of $u_z^{\text{surf}}(\mathbf{r}, t)$, is obtained by replacing $\cos \omega t$ by $\sin \omega t$ in eq. (3).

Tsunami energy

Linear wave theory determines the total tsunami wave energy at any time as

$$E_T(t) = \frac{1}{2} \rho_w g \int_{\mathbf{r}} dA(r) \left[E_z^{\text{surf}}(\mathbf{r}, t) \right]^2. \qquad (5)$$

The tsunami energy peaks towards the end of the landslide movement. Unlike the landslide energy E_L, the tsunami energy depends on the entire kinematic history of the landslide. The ratio E_T/E_L quantifies the tsunami generation efficiency of each landslide.

5 COMPARISON WITH DAMAGE OBSERVATIONS

Close-in damage comparisons

To compare model predictions with after-the-fact damage observations, we use maps of the wave envelope. Fig. 5 shows predicted tsunami envelopes at 2–11 min after the start of the 40 m s^{-1} landslide of Fig. 4. Despite having given just 8 per cent of its gravitational energy to the tsunami, this landslide pushed waves up to several tens of metres off the coasts of Sakar and Umboi. Although these values substantially exceed the 15 m elevation of the devastation zones seen there, we argue that waves of the predicted size would be required immediately offshore to produce the observed damage. First, these short-period waves would lose a lot of energy offshore crashing on to and transiting fringing reefs. Damage accounts on the west coast
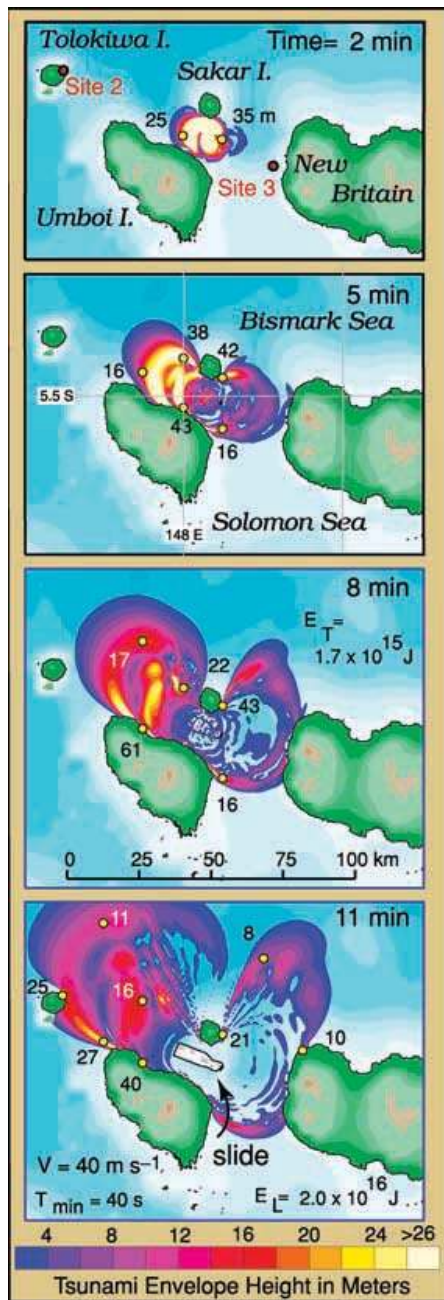
Figure 5. Tsunami envelope heights predicted for the Ritter Island collapse at 2, 5, 8 and 11 min after initiation of the 40 m s^{-1} event. Note that the strongest waves are directed northwestward toward Tolokiwa Island. The numbers list wave height in metres at selected locations (yellow dots).

made (Cooke 1981), probably understate actual inundation heights, which may have been in excess of 20 m.

In contrast to the reports from Sakar and Umboi, damage on the coast of New Britain was examined close up during the rescue of survivors from an expedition that the tsunami almost wiped out. The group measured a 12–15 m elevation of inundation there directly from tidemarks on standing trees. Fig. 5 predicts somewhat larger, 20 m waves offshore New Britain, but we do not consider this a significant discrepancy. The difference attributes to the short wave periods and the loss of wave energy on the offshore reefs and in coastal trees.

We infer, along with Johnson (1987) that damage to the west of Ritter Island was greater than to the east on the coast of New Britain. Our tsunami models focus wave energy in the direction of landslide motion and reproduce this damage pattern. The bright colours in Fig. 5 highlight the wave amplification toward the northwest where islands as far away as Tolokiwa suffer more than the closer western coast of New Britain.

Distant damage comparisons

Fig. 6 evolves the tsunami from 15 to 45 min. The directional nature of the waves is evident here too, with envelope heights substantially less in deep water to the northeast than in deep water to the northwest where a strong series of tsunami waves impact islands as far distant as Manus. Future mapping of tsunami deposits there may reveal whether this is the case. To the northeast, deep water waves of 2 m or so in the eastern Bismarck Sea broadly coincide with the 4.5 m of runup observed at Matupi, the peninsula on the eastern side of Rabaul Harbour (Fig. 1). The limitations of the single-ray approach in the tsunami calculation show in Fig. 6 where nearly the entire coast of New Guinea has been shadowed.

Damage predictions of alternative velocity models

To contrast the results of the 40 m s^{-1} landslide model, the top and bottom groups of Fig. 7 picture the predicted tsunami envelopes at 8 and 11 min for slower (20 m s^{-1} upper frames) and faster (80 m s^{-1} lower frames) slide velocities. The 5–6 m shallow water wave heights produced by the slower landslide fall significantly short of the 12–15 m inundation elevations in western New Britain. Generating tsunami with just 2 per cent efficiency, the 20 m s^{-1} landslide does not seem capable of delivering enough damage. On the other hand, the 80 m s^{-1} landslide model, with a tsunami efficiency of 11 per cent, produces waves off western New Britain that appear too large in view of the relatively well-constrained inundation height and distance there. Even given the limitations of the damage observations on Umboi and Sakar discussed above, the wave heights offshore of these islands for the 80 m s^{-1} model look excessive. The 40 m s^{-1} landslide velocity model fits the damage data better than either of the other two models.

6 COMPARISON WITH EYEWITNESS OBSERVATIONS

We compare direct eyewitness reports of the wave with synthetic tsunami waveforms (Fig. 8) at four proxy locations indicated by the red dots in the first frames of Figs 5 and 6. Site 1, the proxy for Hatzfeldhafen, is located 60 km northeast in 1300 m of water. Sites 2 and 3 correspond to shallower (640 and 260 m) water locations off the coasts of Tolokiwa and New Britain. Site 2 is a partial proxy
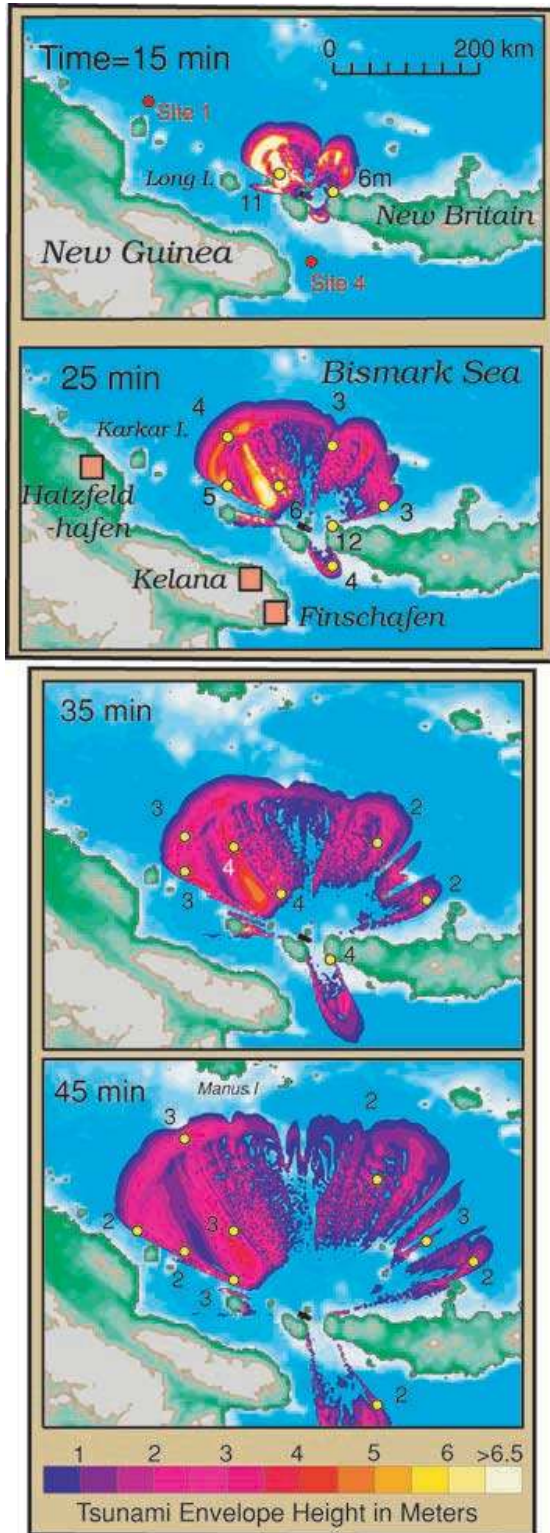
of New Britain do note an abundance of ripped-up coral clasts and other debris from offshore (Cooke 1981), so considerable energy must have been lost to seabed erosion before the wave beached. Secondly, the coastal topography is generally shallowly inclined and heavily vegetated. Resistance of the forest trees and the limited time during which each wave crest had to surge inland before drainback, minimize the zones of devastation. Finally, the inland and upslope limit of the zone of devastation as perceived from the sea, from where the observations of Sakar and Umboi islands were

Figure 6. Tsunami envelope heights predicted for the later stages of the Ritter Island collapse event. The panels show the wave evolution from 15 to 45 min after the start of the 40 m s^{-1} event.
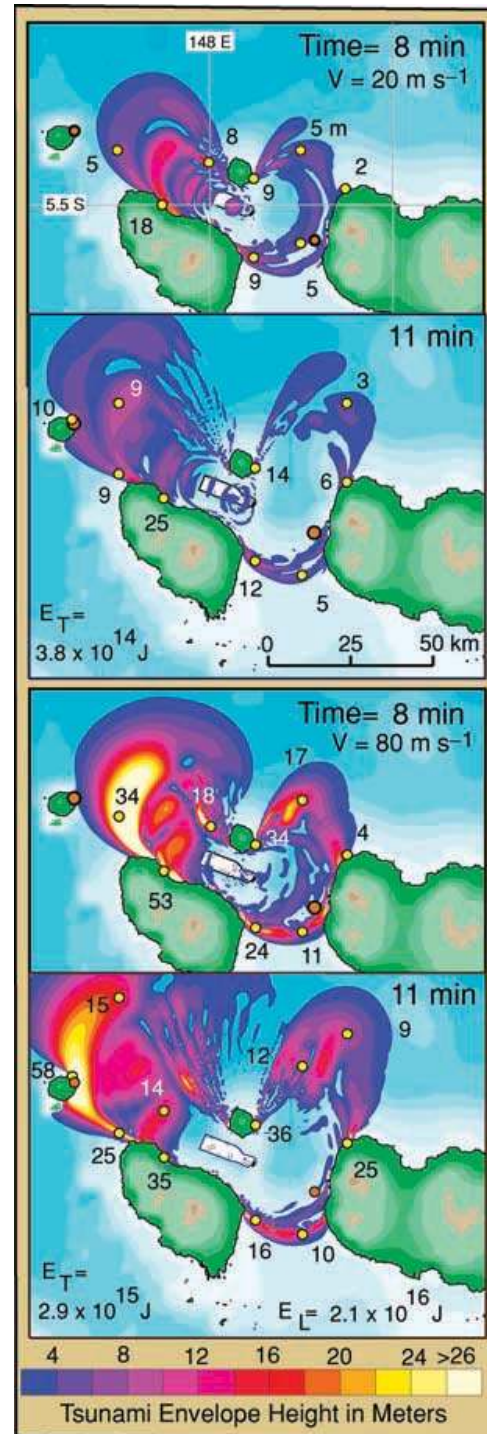

Figure 7. Tsunami envelope heights predicted for the early stages of the Ritter Island tsunami with alternative landslide velocities. The top and bottom groups are for 20 and 80 m s^{-1} slides.

for Kelana, which may have received waves that had travelled both east and west of Umboi. Site 4 is located in deep (3200 m) water south of the Dampier Strait. Waves would have propagated from here to Finschafen and possibly to Kelana. To make a comparison with onshore observations, the waveforms at the deep water proxy sites were shoaled to a hypothetical shallow water ($h(r) \sim 30$ m)
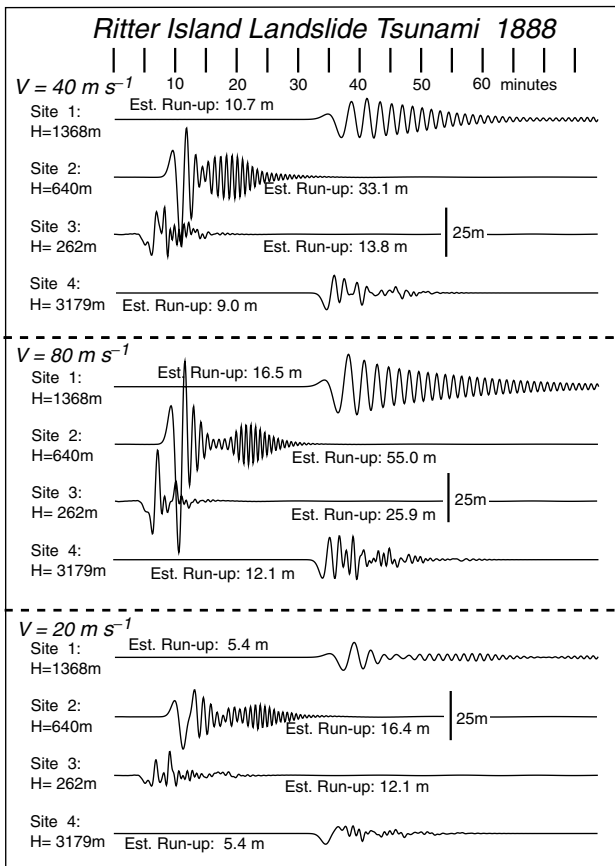
Figure 8. Synthetic tsunami wave trains from 20, 40 and 80 m s^{-1} land-slides at the four offshore proxy sites indicated by red spots in Figs 5 and 6. *H* denotes the actual water depth at the site. To estimate wave size on a hypothetical shores at these sites, shoaling corrections to shallow water have been included and a runup height was predicted using eq. (6). The time in minutes after the start of the landslide is marked along the top.

depth. Then, the amplitudes $A(r)$ of these shoaled waves were scaled to a runup height $\mathcal{R}$ by (Ward & Asphaug 2003)

$$\mathcal{R} = A(\mathbf{r})^{4/5} h(\mathbf{r})^{1/5}. \qquad (6)$$

Wave initial motion

The simulation correctly predicts an initial drop of sea level at Finschafen (Site 4) and an initial rise at Hatzfeldhafen (Site 1). Dipole first motions like this are typical in landslide-generated tsunami—the first wave in the direction of land sliding is positive, whereas in the opposite direction the first wave, generated by draw-down over the excavation is negative.

Wave periods and tsunami duration

Recall that all observers emphasized a 3–4 min wave period. Inspection of the maregrams in Fig. 8 reveals that waves of this period indeed dominate everywhere and confirms that the tsunami originated from the landslide. Fig. 9 plots the amplitude spectrum for each of the records in Fig. 8. Virtually all the tsunami energy lies between 1 and 5 min periods. In the forward direction, toward Sites 1 and 2, the peak near 3 min matches the timed period at Hatzfeldhafen. The fact that 3 min waves also dominate at Kelana suggests
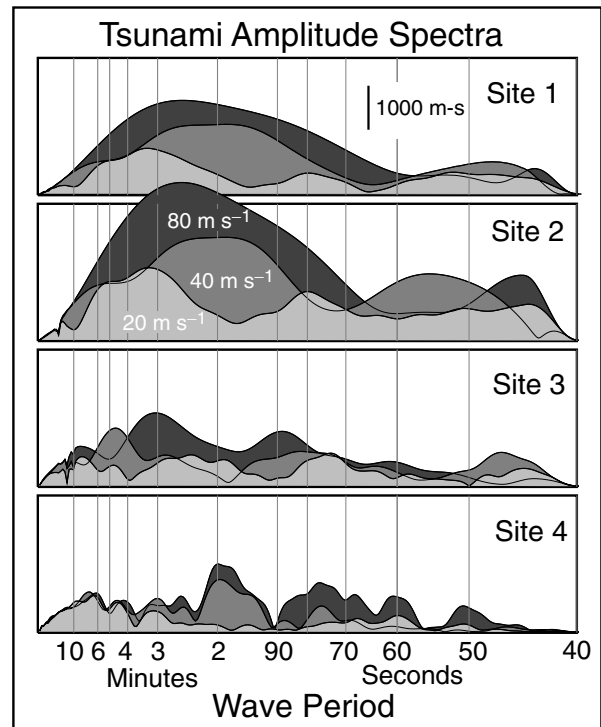

Figure 9. Amplitude spectra of the tsunami waveforms in Fig. 8. Contrast the smooth broad peaks in the spectra at fore-Sites 1 and 2 and complex spectra at back-Sites 3 and 4.

that much of the wave energy arriving there travelled via the channel west of Umboi, rather than via Dampier Strait. Note that fore-Sites 1 and 2 show orderly spectra that become relatively enhanced at short period as the slide velocity increases. In contrast, the back-Sites 3 and 4 show chaotic spectral changes to different landslide speeds. The orderly versus chaotic appearance shows in the records of Fig. 8 as well. Site 4 gives a good qualitative match with the irregular water movements at Finschafen.

The increasing duration of the wave trains (15, 25, 40, >50 min) with increasing distance (in the order Site 3, Site 2, Site 4, Site 1) in Fig. 8 is a consequence of wave dispersion. While unaccounted for reflections and reverberations would extend the duration of actual waves, we suggest that dispersion principally causes the longer duration tsunami at distant Hatzfeldhafen (2.5 h) than closer in at Kelana or Finschafen (1 h and 30 min, respectively).

Time to maximum wave height

The synthetic waveforms at the fore-Sites 1 and 2 predict maximum wave heights close to the beginning of the wave trains. Back-sites to the southeast show the third or fourth wave being the highest. This pattern seems consistent with the observation that the fourth wave was the highest at Kelana, although as noted above, the wave period data indicate a western origin for the waves there.

The most unusual eyewitness observation was that tsunami height peaked at Hatzfeldhafen at about 8 AM, over an hour after the first waves arrived. A notable feature of the synthetic waveforms in Fig. 8 (also evident in Fig. 6) is that a second peak in wave height follows the first by an interval that varies with landslide velocity and distance from the source. This second peak is most evident to the north and west (fore-Sites 1 and 2) in the direction of landslide motion. The

delayed second peak in amplitude corresponds to a second peak in the wave spectra at 45–55 s. The second peak clearly registers in the 40 and 80 m s^{-1} spectra in Fig. 9. The waves in the second peak travel more slowly than the dominant 3 min waves and hence lag behind. Although the second spectral peak is much weaker than the first, it is possible that the harbour at Hatzfeldhafen resonated to the later arriving, shorter-period waves to produce the 1 h delay in maximum wave height. Harbour resonance cannot be evaluated with the presently available data, but because no similar effect occurred elsewhere, the late peak in tsunami size at Hatzfeldhafen must be due to local conditions.

Wave heights

Wave heights computed at the proxy sites should exceed those at mission sites that did not have line-of-sight exposure. Thus, the 8–10 m waves seen at Kelana and Hatzfeldhafen, should correspond to >10 m waves shoaling at the proxy sites. The 20 m s^{-1} landslide of Fig. 8 bears waves much smaller than 10 m at Sites 1 and 4 and not much larger at Site 2, closer to the source than Kelana. A landslide travelling at 20 m s^{-1} does not seem potent enough to produce waves as large as those observed at Kelana and Hatzfeldhafen. Conversely, waves produced from the 80 m s^{-1} landslide appear too large at all distances, even allowing for spreading, dispersion and refraction. We conclude that the most plausible source for the 1888 Ritter Island tsunami waves is a landslide travelling at least 40 m s^{-1}. Velocities of 80 m s^{-1} do not fit the data well, but cannot be excluded.

It should be noted that our model assumes a landslide volume at the upper end of the range proposed by Johnson (1987). In terms of tsunami production, landslide velocity and volume are broadly interchangeable if the plan form of the slide remains similar. Thus, a smaller, thinner landslide produces tsunami comparable to a slower, thicker landslide. Although we doubt that landslide volume shortfalled 4–5 km^3, we cannot exclude a landslide velocity as high as 80 m s^{-1} if it did.

7 SIMPLE MODELS OF LANDSLIDE MECHANICS

We argue above that the observed 1888 Ritter Island tsunami requires a landslide velocity of 40 m s^{-1} or more. Is this speed realistic? Direct data on the speed of volcano collapses are sparse, but analogues exist in large rapid rock avalanches and landslides common to both volcanic and non-volcanic mountains. Remarkably, in relation to the vertical height through which they drop, these landslides and avalanches often runout great distances over gently inclined ground. The ratio of drop height to runout distance h_0/x_c, decreases with landslide volume and ranges between 0.07 to 0.2 for Ritter Island-sized (1–10 km^3) subaerial landslides (Hayashi & Self 1992). Small h_0/x_c ratios require an efficient mechanism to reduce the resistance to landslide motion; that is, to induce a low effective coefficient of basal friction. Debate on the nature of this mechanism continues (see reviews by Hsü 1978; Kilburn 2001), but in debris avalanches (the latter stages of sliding in our model) it is widely attributed to fragment collisions in the rapidly deforming basal layer. Collisions keep fragments apart for most of the time and reduce frictional losses compared with fragments sliding past one another in contact. Earlier on, when the landslide moves as large blocks, an equivalent mechanism operates through development of a pressurized and fluidized fault gouge breccia on basal slip surfaces (Day 1996). With low basal friction, slides once started, acceler-

ate rapidly on initially steep slopes and attain a high velocity early. Rapid initial acceleration is consistent with the observed movement histories of both volcanic (Voight 1981; Voight *et al.* 1983) and non-volcanic (Voight 1978) landslides and rock avalanches. Perhaps the most minutely characterized example is the 1980 May 18 collapse of Mount St Helens. This event began with slide blocks that accelerated to speeds of over 50 m s^{-1} within 26 s and 700 m of the start time and location, respectively (Voight 1981; Voight *et al.* 1983).

To quantify these thoughts, consider the simplest landslide model that contains a basal friction term—the standard sliding block (for example, Ui *et al.* 1986). This model fixes block acceleration $a(x)$ as the gravitational acceleration less the frictional acceleration,

$$a(x) = g[\sin\beta(x) - \mu\cos\beta(x)] = g[\tan\beta(x) - \mu]\cos\beta(x)$$
$$\approx -g[dh(x)/dx + \mu]. \tag{7}$$

Here, $h(x)$ is the slope profile shape and $\beta(x)$ is its slope angle. For subaerial slides, μ is the coefficient of basal friction. For submarine slides, μ can be considered a coefficient of 'effective' friction that includes true basal friction plus all other loss mechanisms (viscous dissipation, energy transfer to waves, etc.). Integrating the approximate version of formula (7) yields the block velocity directly as a function of the slope profile,

$$v(x) = \left[2\int_0^x a(\hat{x})\,d\hat{x}\right]^{1/2} = \sqrt{2g}[h_0 - h(x) - \mu x]^{1/2}. \tag{8}$$

The slide hits peak velocity at position x_p where $\partial h(x_p)/\partial x = -\mu$. Smooth exponential curves

$$h(x) = h_0 e^{-\xi x} \quad \text{with} \quad \xi = \tan\beta_0/h_0 \tag{9}$$

characterize many volcano shapes (Gee *et al.* 2001) with β_0 being the initial slope (see Fig. 10). Shape (9) yields landslide velocity and traveltime as a function of distance:

$$v(x) = \sqrt{2gh_0}\left[1 - e^{-\xi x} - \mu x/h_0\right]^{1/2}; \qquad t(x) = \int_0^x \frac{d\hat{x}}{v(\hat{x})}. \tag{10a,b}$$

The runout distance x_c and slide duration are found by solving

$$x_c = (h_0/\mu)\left[1 - e^{-\xi x_c}\right] \approx (h_0/\mu) \tag{11}$$

then evaluating $t_c = \int_0^{x_c} \frac{d\hat{x}}{v(\hat{x})}$. The mean velocity is defined by the ratio of x_c to t_c, whereas the peak velocity at $x_p = \ln(\tan\beta_0/\mu)/\xi$ is just the free-fall speed times a number less than one,

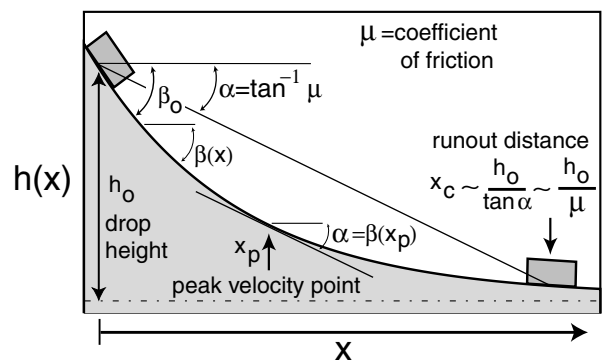$$v(x_p) = \sqrt{2gh_0}\{1 - (\mu/\tan\beta_0)[1 + \ln(\tan\beta_0/\mu)]\}^{1/2}. \tag{12}$$

Figure 10. Sketch of a simple sliding block and parameters in a landslide model. For low friction slides, $\mu \sim h_0/x_c$.
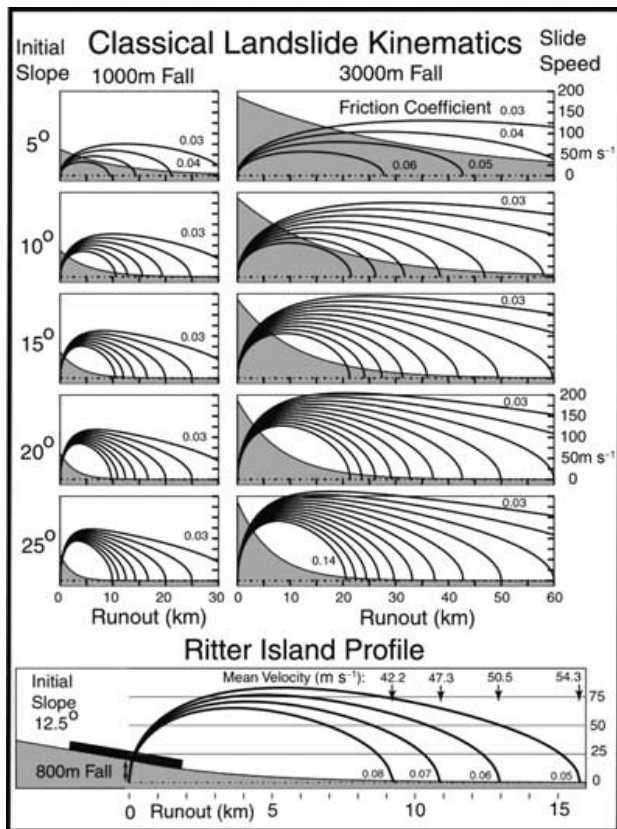
Figure 11. Simple model of landslide block dynamics. In the top panels, the coefficient of effective friction start at 0.03 and increase by 0.01 unit. The bottom panel is the Ritter Island profile.

Fig. 11 graphs velocity (10a) for landslides (9) with various μ descending 1 and 3 km on slopes with $\beta_0 = 5°–25°$. These drop heights approximate, respectively, an island arc stratovolcano such as Ritter and a moderate-sized oceanic island volcano. Unsurprisingly, slides accelerate faster on volcanoes with steeper upper slopes and at lower effective friction coefficient. In all of the cases considered here, the landslide attains peak velocity early and follows a gradual deceleration as it runs out. Rapid landslide acceleration enhances tsunami production because waves generate most efficiently when slides move in water not much deeper than their thickness and at speeds approaching the $\sqrt{gh}$ wave velocity (Tinti *et al.* 2001; Ward 2001).

The lower panel of Fig. 11 traces velocity histories and runout distances for a fall height (800 m) and an initial slope angle (12.5°) similar to the 1888 landslide with various effective μ values. Although we do not have a direct measurement of the runout extent of the Ritter Island debris avalanche, the absence of almost all of the deposit within from the area surveyed by Johnson implies a minimum distance of 8 km. According to Fig. 11, a 8 km runout corresponds to an effective μ of about 0.07. The fact that the effective μ for the submarine Ritter Island slide is on the low end of the values measured in subaerial slides, confirms that basal friction is the principal mechanism for restricting the speed of submarine landslides—not viscous losses or energy lost to wave generation. (We already know that the latter is just a few per cent.)

From the known geometry of the Ritter Island debris field, the block mechanical model (5) predicts that the landslide had a

mean velocity of around 40 m s^{-1} (peak velocity near 70 m s^{-1}) and would have reached its mean velocity in the first kilometre of movement (less than the size of one of the cells of Fig. 4). The agreement of these independently predicted speeds with the 40+ m s^{-1} rates needed to fit tsunami observations is compelling to us.

If viewed in the perspective of much larger flank collapses, a 40 m s^{-1} speed for the Ritter Island landslide is far from excessive. For instance, the Nuaanu landslide (5000 km^3) must have been running at more than 80 m s^{-1} for it to climb 350 m up the far slope of the Hawaiian flexural trough (Ward 2001). The higher speed achieved in larger collapses such as La Palma or Kilauea result mostly from the greater distance through which landslides on the flanks of oceanic islands descend compared with stratovolcanos. For a fixed initial slope and coefficient of friction, eq. (11) says that the peak landslide velocity increases with the square root of the drop height. Ritter-sized events ($h_0 = 800$ m) should hit speeds only about half as fast as collapses that fall 3000 m. Compounding this, because the particle interaction mechanism that reduces basal friction works better at high velocity, the effective μ itself decreases with drop height. This, in turn, increases the slide speed. After falling from oceanic island volcanoes, giant landslides might run at velocities >100 m s^{-1}—the type of speeds used for our Kilauea and La Palma models (Ward & Day 2001; Ward 2002a).

We can test the reasoning for high-speed landslides more closely by breaking out of eq. (7) a specific viscous dissipation term

$$a(x) \approx -g[dh(x)/dx + \mu_1] - \mu_2 v^2(x), \qquad (13)$$

where μ_2 is the coefficient of viscous friction and μ_1 is now the coefficient representing all other mechanisms. Perhaps a strong velocity-squared dissipation caps landslide speeds to much lower values than predicted by eq. (7)? For landslides such as Ritter and La Palma, the friction coefficients in eq. (13) cannot be selected independently because the ratio of fall height to run out distance is known. Thus, any extra μ_2 dissipation must come with a reduction of μ_1 dissipation, otherwise the slide would stop prematurely. The solid curves in Fig. 12 follow velocity trajectories obtained by integrating eq. (13) with $\mu_1 = 0.07$ and $\mu_2 = 0$ for the Ritter Island slide (bottom of Fig. 11) and for a La Palma-type slide. The dashed curves in Fig. 12 trace the velocity trajectories when μ_2 is increased to 8×10^{-5} and 8×10^{-6} m^{-1}, while μ_1 falls to maintain a constant runout distance. In all cases, the block accelerates faster, but reaches a lower peak velocity with a non-zero μ_2. Harbitz (1992) proposed that the viscous friction coefficient take the form

$$\mu_2 \approx \frac{\rho_w c_d}{2\rho_s \Delta u}, \qquad (14)$$

where Δu is the slide thickness and

$$C_d = [1.89 + 1.62 \log(L/k)]^{-5/2}. \qquad (15)$$

In eq. (15), L equals the block length and $k = 0.01–0.1$ m. Taking $\rho_w/\rho_s = 1/2.5$ and $L = 5000$ m, $\Delta u = 50$ m for Ritter Island and $L = 15\,000$ m, $\Delta u = 1000$ m for La Palma, the respective viscous coefficients, eq. (14), are $(1.0–1.4) \times 10^{-5}$ and $(4.1–5.9) \times 10^{-7}$ m^{-1}. The uppermost dashed curves in Fig. 12 use $\mu_2 = 10^{-5}$ and $\times 10^{-6}$ m^{-1} and induce about a 10 per cent velocity reduction over the case where $\mu_2 = 0$. We believe that, even in the presence of plausible degrees of viscous dissipation, giant landslides such as La Palma run at speeds exceeding 100 m s^{-1}.
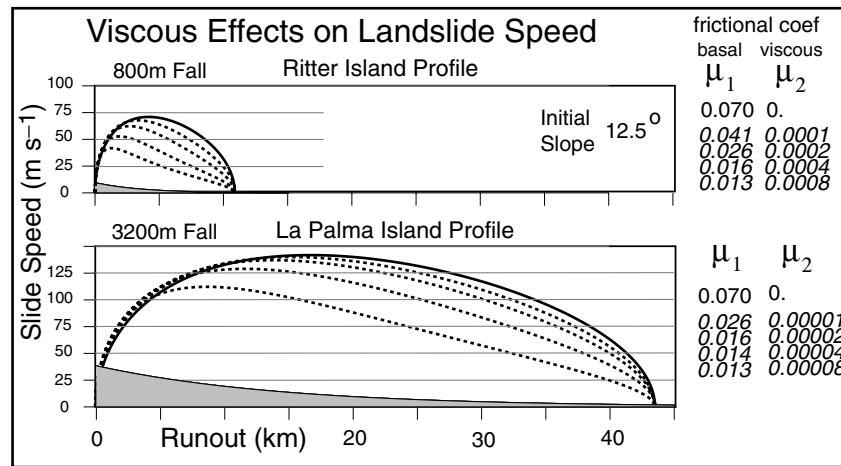
Figure 12. Velocity trajectories of Ritter Island (top) and La Palma type (bottom) landslides with ($\mu_2 > 0$, dashed lines) and without ($\mu_2 = 0$, solid line) viscous dissipation as computed from eq. (13). Uppermost two dashed lines represent the most plausible μ_2 values. The grey area is the slope profile. Giant landslides such as La Palma should run at speeds exceeding 100 m s^{-1} even in the presence of viscous dissipation.

8 CONCLUSIONS

Although a unanimous verdict is impossible due to the limited data available, we judge this landslide tsunami model to be successful in reproducing the observed features of the 1888 Ritter Island tsunami. The successful model used fully reasonable collapse geometries, volumes and kinematics that are consistent with actual bathymetric data and theories of landslide mechanics. Our study highlights the importance of short- (1–5 min) period tsunami waves that small (1–100 km^3) landslides produce and the need for frequency dispersion to be included in modelling their propagation. Importantly, we find that these short-period tsunami waves, commonly disregarded as a quickly dispersing local hazard, are in fact capable of carrying damaging and potentially deadly energy to several hundred km.

Deposits from the 1888 Ritter Island landslide and tsunami represent a living laboratory for investigating volcano-collapse-generated tsunami. Information discovered in this laboratory immediately apply to tsunami hazards associated with similar size stratovolcanoes elsewhere, and through scaling, to the much greater hazards posed by collapses of oceanic island volcanoes. These computer simulations have pinpointed three areas of future fieldwork in the Ritter Island laboratory that would be particularly rewarding: (1) mapping of the landslide deposit and collapse scar using modern multibeam bathymetric and backscatter imaging sonars coupled with shallow reflection seismic profiling; (ii) detailed charting and sedimentological characterization of tsunami deposits on Sakar, Tolokiwa, Umboi, western New Britain and even Manus; and (iii) systematic collection of still extant oral and written histories of the 1888 collapse from people around the Dampier Strait and from more distant islands to the northwest.

With regard to the tsunami models, improved versions are expected that will allow waves to travel on indirect paths to coastlines without a line of sight to the landslide source. Even in its present form, the success in reproducing the features of the 1888 Ritter Island tsunami further affirms that our approach embraces all of the key physical features of landslide tsunami generation. We see nothing in this experiment that suggests a fault in our previous predictions of transoceanic mega-tsunami generated by oceanic island collapses 100 or 1000 times larger in scale.

REFERENCES

Aida, I., 1978. Reliability of a tsunami source model derived from fault parameters, *J. Phys. Earth,* **26,** 57–73.

Cooke, R.J.S., 1981. Eruptive history of the volcano at Ritter Island, in *Cooke–Ravian Volume of Volcanological Papers,* pp. 115–123, ed. Johnson, R.W., Geological Survey of Papua New Guinea Memoir 10.

Davies, H.L., Davies, J.M., Perembo, R.C.B. & Lus, W.Y., 2003. The Aitape 1998 tsunami: reconstructing the event from interviews and field mapping, *Pure Appl. Geophys.,* **160,** in press.

Day, S.J., 1996. Hydrothermal pore fluid pressure and the stability of porous, permeable volcanoes, in *Volcano Instability on the Earth and Other Planets,* pp. 77–93, eds McGuire, W.J., Jones, A.P. & Neuberg, J., Geological Society of London Special Publication, 110.

Gee, M.J.R., Watts, A.B., Masson, D.G. & Mitchell, N.C., 2001. Landslides and the evolution of El Hierro in the Canary Islands, *Mar. Geol.,* **177,** 271–293.

Hayashi, J.N. & Self, S., 1992. A comparison of pyroclastic flow and debris avalanche mobility, *J. geophys. Res.,* **97,** 9063–9071.

Harbitz, C.B., 1992. Model simulations of tsunamis generated by the Storegga Slides, *Mar. Geol.,* **105,** 1–21.

Hsü, K.J., 1978. Albert Heim: observations on landslides and relevance to modern interpretations, in *Rockslides and Avalanches 1. Natural Phenomena,* pp. 71–93, ed.Voight, B., Elsevier, New York.

Johnson, R.W., 1987. Large-scale volcanic cone collapse: the 1888 slope failure of Ritter volcano, *Bull. Volcanol.,* **49,** 669–679.

Johnson, J.M. & Satake, K., 1996. The 1965 Rat Islands earthquake: a critical comparison of seismic and tsunami wave inversions, *Bull. seism. Soc. Am.,* **86,** 1229–1237.

Kanamatsu, T., Herrero-Bervera, E. & McMurtry, G.M., 2002. Magnetostratigraphy of deep-sea sediments from piston cores adjacent to the Hawaiian Islands: implications for ages of turbidites derived from submarine landslides, in *Hawaiian Volcanoes: Deep Underwater Perspectives,* eds Takahashi, E., Lipman, P.W., Garcia, M.O., Naka, J. & Aramaki, S., AGU Geophysical Monograph Series, 128, Section 1.

Kawata, Y. *et al.,* 1999. Tsunami in Papua New Guinea was as intense as first thought, *EOS, Trans. Am. geophys. Un.,* **80** 101 104–105.

Kilburn, C.R.J., 2001. The flow of giant rock landslides, in *Paradoxes in Geology,* pp. 245–265, eds Briegel, U. & Xiao, W., Elsevier, Amsterdam.

Latter, J.H., 1981. Tsunamis of volcanic origin; summary of causes, with particular reference to Krakatoa, 1883, *Bull. Volcanol.,* **44,** 467–499.

McSaveney, M.J., Goff, J.R., Darby, D.J., Goldsmith, P, Barnett, A., Elliot, S. & Nongkas, M., 2000. The 17 July 1998 tsunami, Papua New Guinea; evidence and initial interpretation, *Mar. Geol.,* **170,** 81–92.

Satake, K., 1987. Inversion of tsunami waveforms for the estimation of a fault heterogeneity: method and numerical experiments, *J. Phys. Earth,* **35,** 241–254.

Satake, K. & Kato, Y., 2001. The 1741 Oshima–Oshima eruption: extent and volume of submarine debris avalanche, *Geophys. Res. Lett.,* **28,** 427–430.

Satake, K., Smith, J.R. & Shinozaki, K., 2002. Three-dimensional reconstruction and Tsunami model of the Nuuanu and Wailau Giant Landslides, Hawaii, in *Hawaiian Volcanoes: Deep Underwater Perspectives,* eds Takahashi, E., Lipman, P.W., Garcia, M.O., Naka, J. & Aramaki, S., AGU Geophysical Monograph Series, 128, Section 3.

Self, S. & Rampino, M.R., 1981. The 1883 eruption of Krakatau, *Nature,* **294,** 699–704.

Siebert, L., Glicken, H. & Ui. T., 1987. Volcanic hazards from Bezymianny and Bandai-type eruptions, *Bull. Volcanol.,* **49,** 435–459.

Simkin, T. & Fiske, R.S., 1983. *Krakatau 1883: the Volcanic Eruption and its Effects,* Smithsonian Institute Press, Washington, p. 464.

Tinti, S., Bortolucci, E. & Chiavettier, C., 2001. Tsunami excitation by submarine slides in shallow-water approximation, *Pure Appl. Geophys.,* **158,** 759–797.

Ui, T., Yamamoto, H & Suzuki-Kamata, K., 1986. Characterization of debris avalanche deposits in Japan, *J. Volc. Geotherm. Res.,* **29,** 231–243.

Voight, B., ed. 1978. *Rockslides and Avalanches 1: Natural Phenomena,* Elsevier, Amsterdam, p. 833.

Voight, B., 1981. Time scale for the first moments of the May 18 eruption, in *The 1980 Eruptions of Mount St Helens, Washington,* pp. 69–86, eds Lipman, P.W. & Mullineaux, D.R., US Geol. Surv. Prof. Paper 1250.

Voight, B., Janda, R.J., Glicken, H. & Douglass, P.M., 1983. Nature and mechanics of the Mount St Helens rockslide-avalanche of 18 May 1980, *Geotechnique,* **33,** 243–273.

Ward, S.N., 2001. Landslide tsunami, *J. geophys. Res.,* **106,** 11 201–11 216.

Ward, S.N., 2002a. Slip-sliding away, *Nature,* **415,** 973–974.

Ward, S.N., 2002b. Tsunamis, in *Encyclopedia of Physical Science and Technology,* Vol. 17, 3rd edn, pp. 175–191, Academic, New York.

Ward, S.N. & Asphaug, E., 2003. Asteroid impact tsunami of 2880 March 16, *Geophys. J. Int.,* **153,** F6–F10.

Ward, S.N. & Day, S.J., 2001. Cumbre Vieja Volcano—potential collapse and tsunami at La Palma, Canary Islands, *Geophys. Res. Lett.,* **28,** 397–400.